
RADIATIVE FORCING BY CO₂ OBSERVED AT TOP OF ATMOSPHERE FROM 2002-2019

A PREPRINT

© Chris Rentsch*
Midland, MI 48642
rentcp@gmail.com

November 5, 2020

ABSTRACT

Spectroscopic measurements at top of atmosphere are uniquely capable of attributing changes in Earth's outgoing infrared radiation field to specific greenhouse gases. The Atmospheric Infrared Sounder (AIRS) placed in orbit in 2002 has spectroscopically resolved a portion of Earth's outgoing longwave radiation for over 17 years. Concurrently, atmospheric CO₂ rose from 373 to 410 ppm, or 28% of the total increase over pre-industrial levels. The Coupled Model Intercomparison Project Phase 6 (CMIP6) multi-model ensemble average predicts 0.477 Wm⁻² clear-sky longwave effective radiative forcing from this increase. Global measurements under nighttime, clear-sky conditions reveal 0.360±0.026 Wm⁻² of CO₂-induced longwave radiative forcing, or 75±5% of model predictions.

Keywords CO₂ · Forcing · Satellite · Infrared · Atmosphere · Measurement

1 Introduction

Increasing infrared absorption caused by rising CO₂ is asserted as the fundamental physical mechanism underpinning anthropogenic global warming. Despite numerous studies of global temperature trends and rising greenhouse gas concentrations, very few investigations offer long-term spectroscopic measurement of CO₂ altering Earth's outgoing longwave radiation (OLR). Harries et al. (2001) qualitatively compared 529 OLR spectra measured in 1970 by the IRIS satellite to 4,061 spectra measured in 1996 by IMG over the Pacific Ocean. Griggs and Harries (2007) examined 25 IRIS, 138 IMG and 37,834 AIRS spectra measured over the central pacific. Feldman et al. (2015) reported increasing downwelling longwave radiation (DLR) in two 1.6° conical upward views of the atmosphere between 2000 and 2010 (figure 1).

None provide a quantitative global assessment of CO₂-induced radiative forcing. The Atmospheric Infrared Sounder (AIRS) offers the longest continuous record among all current or previous satellite spectrometers and has measured Earth's OLR while atmospheric CO₂ concentration rose from 373 to 410 ppm, 28% of the total increase since 1750. Figure 2 exemplifies a single OLR spectrum comprised of 2,378 radiances. This work examines 42.4 billion global nighttime, clear-sky spectral radiance measurements (hereafter: radiances) made by AIRS between 2002-2019.

2 Data

The majority of satellite views of Earth contain clouds that reflect or absorb upwelling infrared (IR). Clear-sky scenes are preferred to avoid attributing cloud-induced OLR reductions to CO₂. The AIRS version 6 level 2 data product (Teixeira, 2013) quantifies fractional cloud content ranging from 0.00 to 1.00 for each radiance measurement. This work utilizes radiances with 0.00 cloud fraction; only 11% of radiances meet this criterion. Although AIRS Level 2 measurements are a cloud-cleared data product, only naturally clear-sky radiances with no mathematical adjustments contribute to this analysis. Figure 3 provides a clear-sky selection example rendered from the sunlit side of Earth

*www.chrisrentsch.com

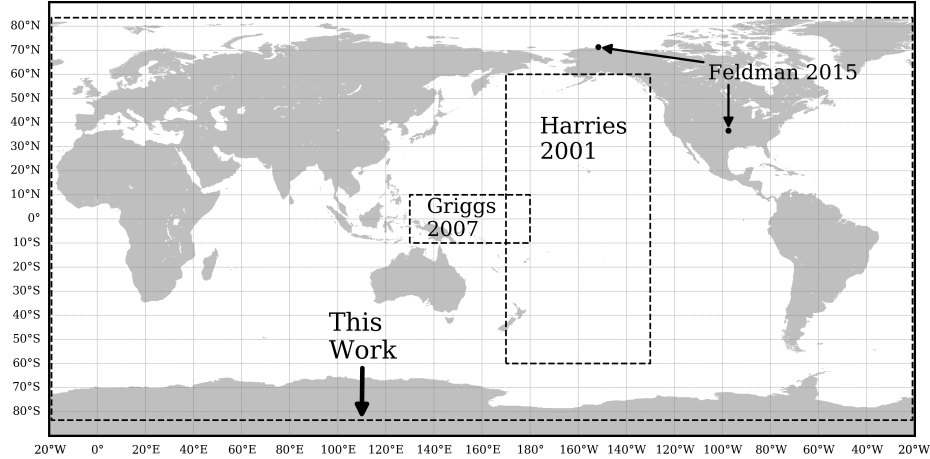


Figure 1: Measurement coverage for this work and select prior works by others

to permit comparison with a visible-wavelength image, however no daytime OLR measurements contributed to this analysis. It is evident that the cloud detection algorithm is conservative: visibly clear areas were not included and no visibly cloud-contaminated areas were inadvertently included (in this example the cloud detection algorithm has false positives but no false negatives).

Solar longwave infrared radiation reflected by clouds or Earth’s surface and combining with terrestrial IR would contaminate daytime OLR measurements. To eliminate this source of error, only nighttime measurements were utilized. When the AIRS solar zenith angle (SZA) is $\leq 90^\circ$ AIRS observes the sunlit side of Earth, when $90^\circ < \text{SZA} < 108^\circ$ it observes the twilight region and when $\text{SZA} \geq 108^\circ$ it observes the nighttime region. Only measurements at $\text{SZA} \geq 108^\circ$ were utilized.

The AIRS mirror scans $\pm 49.5^\circ$ from nadir across flight track. In the bands of radiatively active gasses, higher scan angle observations exhibit limb-brightening or limb-darkening due to IR emission originating higher in the atmosphere. To reduce the effects of this anisotropy, only radiances at scan angles $\leq 15^\circ$ were utilized.

AIRS does not have measurement capability at $< 649.6 \text{ cm}^{-1}$, $1136\text{-}1217 \text{ cm}^{-1}$ or $1614\text{-}2181 \text{ cm}^{-1}$. The 2,378 individual channels comprising the AIRS IR sensor are monitored for quality and only those recommended for scientific use and not subject to static or dynamic noise were utilized. Radiance measurements flagged as dust-contaminated were excluded, though these were rare ($< 0.01\%$).

3 Method

Every AIRS radiance measurement meeting the selection criteria was analyzed in this study (not a subset). The nature of the satellite’s precessing polar orbit characteristically produces fewer equatorial observations and more polar observations than area-proportional to Earth. To generate a spatially-representative dataset, radiances for a given channel in a given month were gridded in 10° latitude x 20° longitude cells. For example, 102 nighttime, clear-sky radiances measured at $0^\circ\text{-}10^\circ\text{S}$ x $20^\circ\text{-}40^\circ\text{E}$ contribute to the 650.814 cm^{-1} average radiance for January 2013 (figure 4, inset). 25.1% of grid cells contain no data due to heavy clouds, lack of nighttime measurements (e.g., polar summers) or failed detector channels. A median of 65 radiances contribute the monthly average for a given channel in a given grid cell. Over time, some detector channels succumb to solar radiation exposure and cease useful data production. Of the maximum potential 17 year record, channels with fewer than four years were excluded for insufficient record length (0.21% of all channels).

A straight line was fit by least-squares regression to the time series of monthly radiance averages for each channel in each grid cell. Seasonal temperature cycles were eliminated as a source of trend bias by utilizing only complete years of measurement data starting on 1 September 2002 and ending on 31 August 2019. An example line fitting is provided in figure 4. The slope of each line is the spectral radiance trend $\frac{dL_{\lambda}}{dt}$ ($\text{mW m}^{-2}(\text{cm}^{-1})^{-1}\text{sr}^{-1}\text{yr}^{-1}$) and the trend uncertainty is $\pm 2.3\text{mK/yr}$, the AIRS instrument stability reported by Strow and DeSouza-Machado (2020). Instrument stability was used instead of the standard error of the regression because the latter is overwhelmingly an indication of seasonality in the radiance time series. A larger uncertainty of $\pm 8\text{mK/yr}$ was utilized at midwave IR channels ($2181\text{-}2665 \text{ cm}^{-1}$) for reasons detailed in sources of error. Lines were fit to monthly averages of all channels

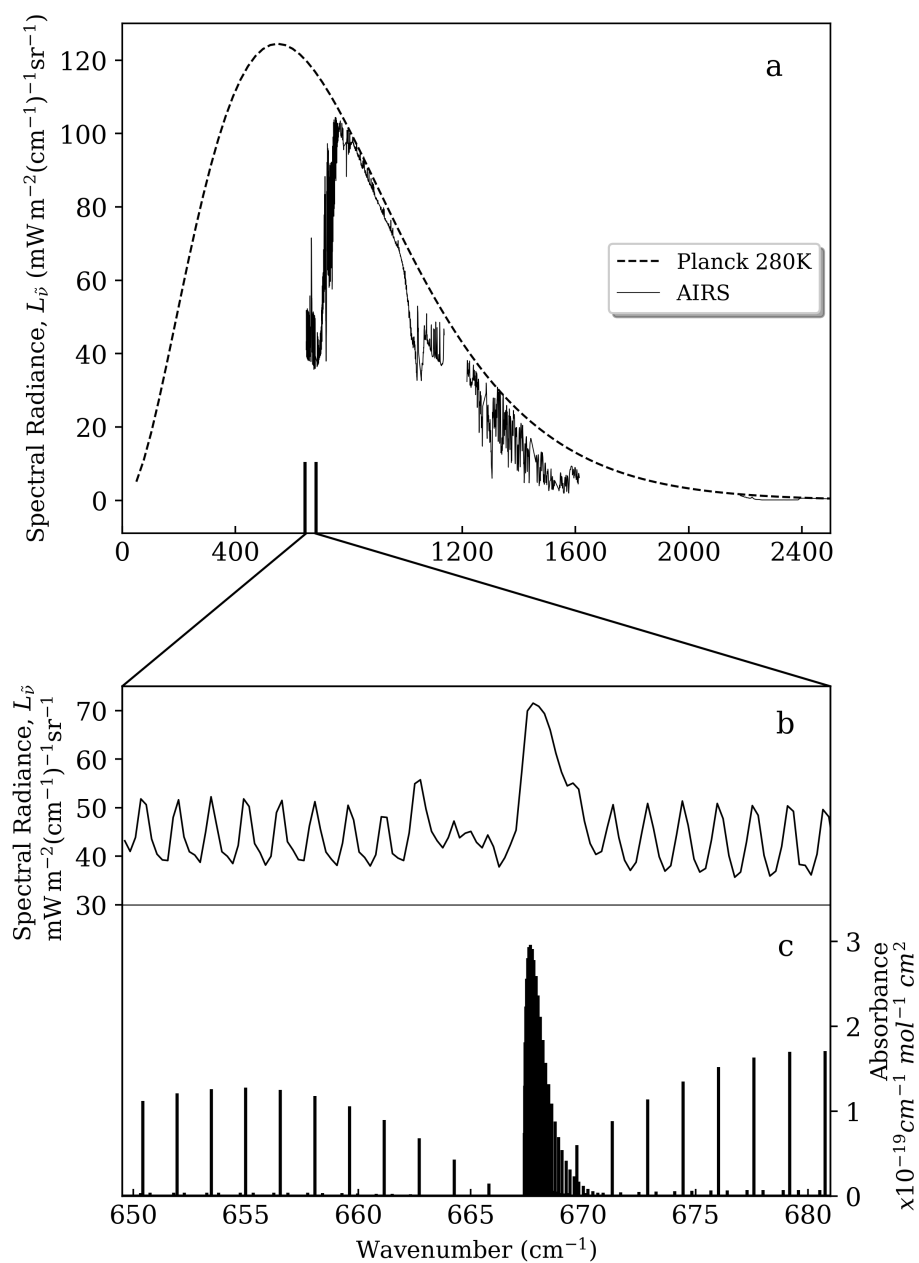


Figure 2: [a] AIRS nighttime, clear-sky OLR spectrum and 280K Planck distribution, [b] 650-680 cm^{-1} subset, [c] HITRAN2016 spectral absorbance lines for CO_2 (Gordon et al., 2017). At wavenumbers where CO_2 is a strong IR absorber, it is also a strong emitter (Kirchhoff's Law) hence the excellent coincidence between detected radiance peaks and HITRAN CO_2 absorbance lines.

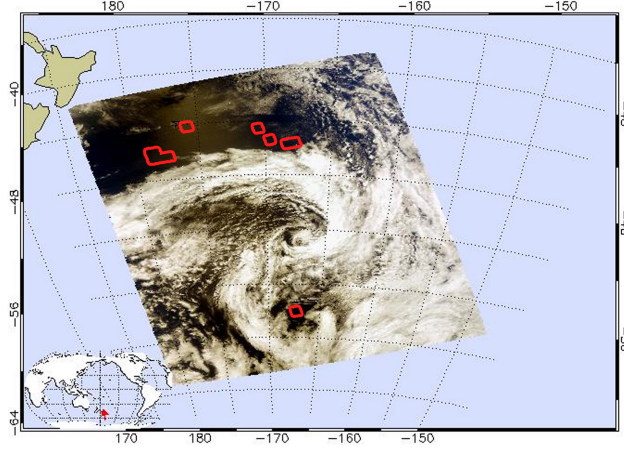


Figure 3: Visible wavelength image collected at 01:29:22 UTC on January 1, 2016. clear-sky regions identified by the cloud detection algorithm outlined in red.

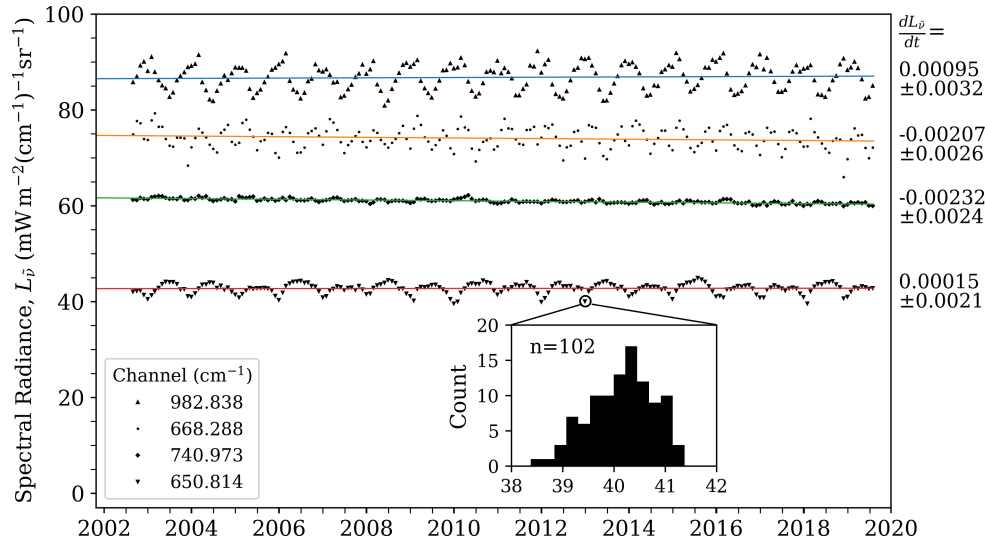


Figure 4: Least-squares regression fit to average monthly radiances for four AIRS channels in 0°-10°S x 20°-40°E grid cell. Remaining channels in all 324 grid cells were fit similarly.

in all 324 grid cells. Area-weighted spectral radiance trends for 10° latitude increments (figure 5) and the global average (figure 6) were constructed therefrom. The scan angle restriction prevents measurement at >83.5°N and <83.5°S therefore polar radiances measured at 80°-83.5° were weighted for 80°-90°.

4 Results: CO₂ Radiative Forcing

OLR reductions in the CO₂ v_2 and v_3 bands are presumed the result of rising atmospheric CO₂ concentration. The reductions at detectable portions of the v_2 band fundamental Q-branch (667 cm⁻¹) and associated P- and R-branches (650-687 cm⁻¹) are relatively minor compared to 687-765 cm⁻¹ where the majority of detectable OLR reduction coincides with the 720 cm⁻¹ Q-branch and associated P- and R-branches, frequently described as a wing. Another Q-branch at 791 cm⁻¹ was also quantified, though its P- and R-branches do not absorb strongly enough to reduce OLR at current CO₂ concentrations. The v_3 asymmetric stretch generates a parallel band with P- and R-branches but no central Q-branch. The C¹²O₂ and C¹³O₂ v_3 bands are centered at 2349 cm⁻¹ and 2284 cm⁻¹, respectively.

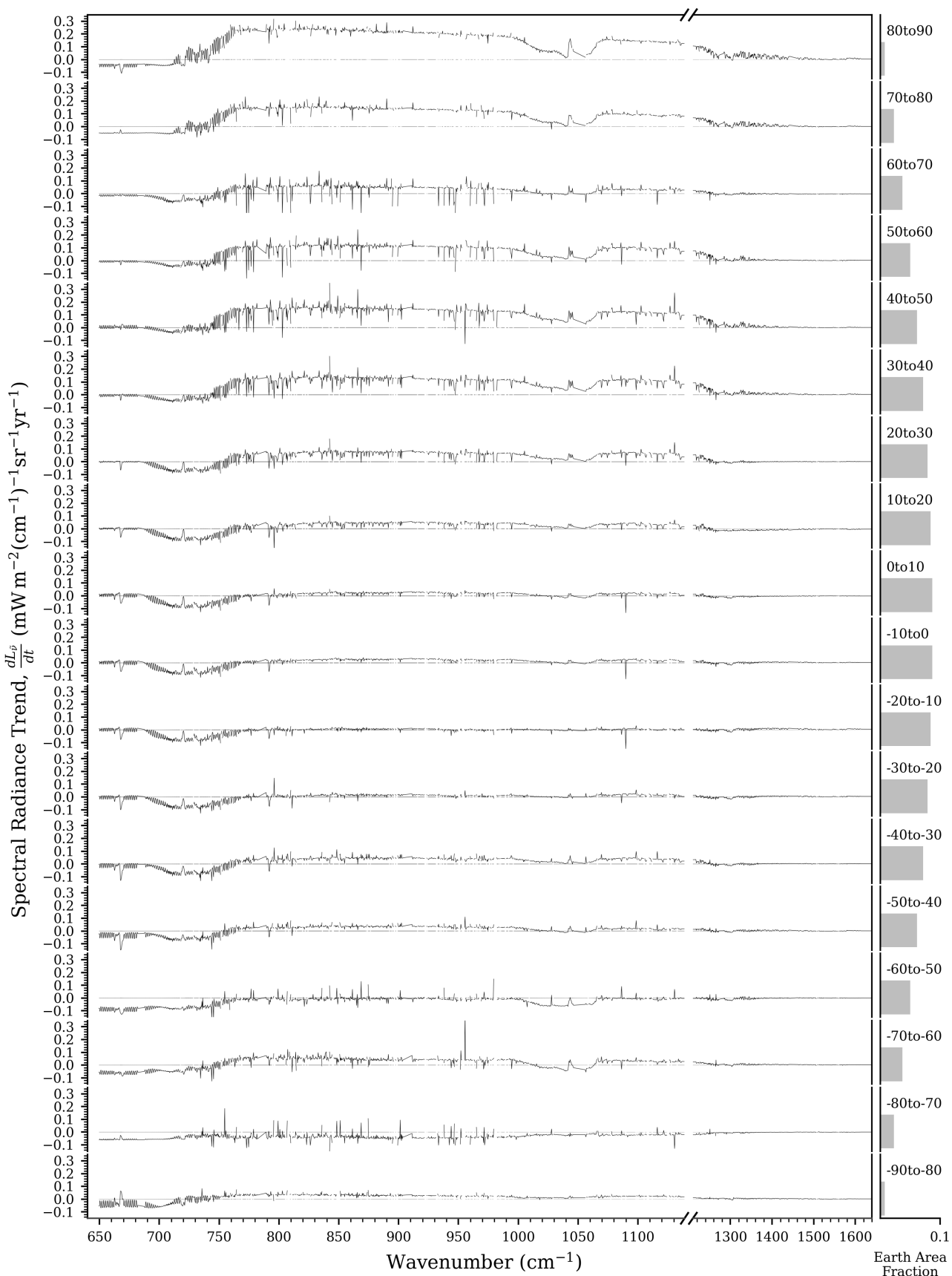


Figure 5: Nighttime, clear-sky spectral radiance trend 2002-2019 in 10° latitude increments. ± 2.3 mK/yr shaded at each abscissa.

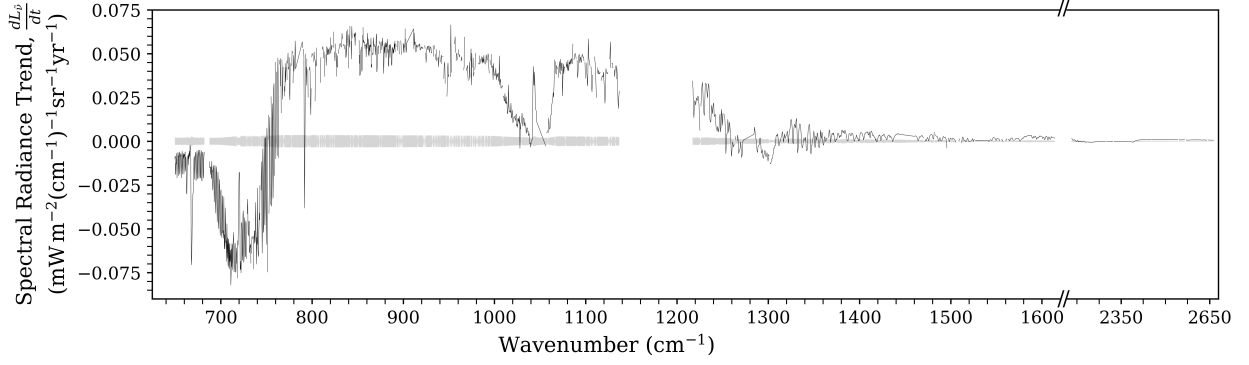


Figure 6: Global composite nighttime, clear-sky spectral radiance trend 2002-2019. ± 2.3 mK/yr shaded at <1614 cm^{-1} and ± 8 mK/yr shaded at >2181 cm^{-1} . OLR reductions attributable to $+37$ ppm CO_2 are evident at <765 cm^{-1} . Increased emission in the atmospheric window 800 - 1000 cm^{-1} is consistent with $\approx 0.3^\circ\text{C}/\text{decade}$ surface warming.

OLR radiant exitance change δM (Wm^{-2}) was produced by integrating the spectral radiance trend ($\frac{dL_{\tilde{\nu}}}{dt}$) over the range of CO_2 -affected wavenumbers and multiplying by 17 years and by π sr, regarding the atmosphere as a Lambertian emitter at these optically-thick channels:

$$\delta M_{v_2PQR} = 17\pi \int_{649.6\text{cm}^{-1}}^{681.7\text{cm}^{-1}} \frac{dL_{\tilde{\nu}}}{dt} d\tilde{\nu} = -0.029 \pm 0.004 \text{ Wm}^{-2} \quad (1)$$

$$\delta M_{v_2wing} = 17\pi \int_{687.6\text{cm}^{-1}}^{764.5\text{cm}^{-1}} \frac{dL_{\tilde{\nu}}}{dt} d\tilde{\nu} = -0.164 \pm 0.011 \text{ Wm}^{-2} \quad (2)$$

$$\delta M_{v_2791} = 17\pi \int_{791.4\text{cm}^{-1}}^{792.5\text{cm}^{-1}} \frac{dL_{\tilde{\nu}}}{dt} d\tilde{\nu} = -0.0008 \pm 0.0003 \text{ Wm}^{-2} \quad (3)$$

$$\delta M_{v_3} = 17\pi \int_{2195\text{cm}^{-1}}^{2396\text{cm}^{-1}} \frac{dL_{\tilde{\nu}}}{dt} d\tilde{\nu} = -0.003 \pm 0.001 \text{ Wm}^{-2} \quad (4)$$

Integrals are depicted in figure 7. At the wing edges in (2) and (4), only reductions in OLR were integrated. A measurement gap between AIRS detector arrays 11 and 12 (681.7 - 687.6 cm^{-1}) was estimated using 676.6 - 681.7 cm^{-1} R-branch measurements. Additionally, fourteen individual failed detector channels were interpolated from adjacent channels prior to integration. The majority of detectable OLR change is attributable to the increasing CO_2 v_2 wing absorption at 687 - 765 cm^{-1} . The symmetrical wing at 575 - 650 cm^{-1} is outside of AIRS measurement range. Consequently, the sum of (1-4) is only a partial measurement of δM caused by rising CO_2 and total δM_{LW} must be estimated. The P-branch and R-branch absorption lines flanking the Q-branch are nearly symmetrical and rising CO_2 caused nearly-identical reductions in radiance. By extension, it is a reasonable prediction that the unmeasured 575 - 650 cm^{-1} wing has undergone OLR reduction by an amount similar to the measured 687 - 765 cm^{-1} wing. The presumption of wing symmetry is supported by several radiative transfer model simulations of top-of-atmosphere (TOA) OLR spectral change after doubling atmospheric CO_2 (Charlock, 1984; Huang and Ramaswamy, 2009; Huang et al., 2010; Brindley and Bantges, 2016). Therefore, total OLR reduction due to rising CO_2 is estimated as:

$$\delta M_{LW} = \delta M_{v_2PQR} + 2\delta M_{v_2wing} + \delta M_{v_2791} + \delta M_{v_3} = -0.360 \pm 0.026 \text{ Wm}^{-2} \quad (5)$$

The uncertainty is taken as the simple sum of the component uncertainties rather than by quadrature as causes of instrument drift are unlikely to be independent and are rather more likely related to a common optical system component (e.g., black body cavity).

5 Comparison to CMIP6

Measurement of the atmospheric CO_2 concentration increase that produced δM_{LW} was supplied by the NOAA ESRL's global monitoring division (Dlugokencky and Tans, 2020). The combination of empirical measurements of RF at TOA and CO_2 concentration change permits comparison to climate model predictions of CO_2 -induced radiative forcing. AIRS TOA measurements contain all infrared responses to surface and atmospheric temperature adjustments, therefore

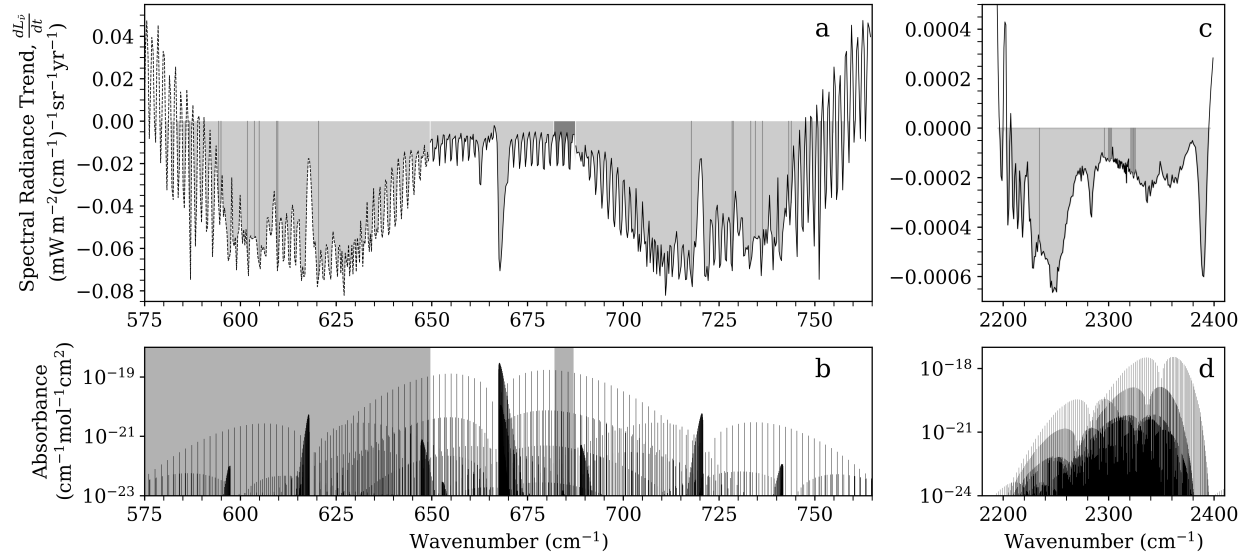


Figure 7: [a] CO_2 ν_2 band spectral radiance trends. Integrated regions shaded: measured values in light gray and interpolations in dark gray. Dashed line at $575\text{-}649\text{ cm}^{-1}$ is $687\text{-}765\text{ cm}^{-1}$ measurements reflected about the 667 cm^{-1} Q-branch. [b] HITRAN 2016 absorption lines for ν_2 band. Shaded regions are where AIRS lacks measurement capability. [c] and [d] are the same as [a] and [b] except for the ν_3 band.

the most suitable comparison is effective radiative forcing (ERF), introduced by Myhre et al. (2013). ERFs calculated by high spectral resolution line-by-line models at fixed surface temperature give no adjustment for increased OLR from the Planck response to surface warming. More computationally-intensive climate models are required to generate ERFs that include surface temperature change, with the trade-off of utilizing a lower spectral resolution (Etminan et al., 2016). Most climate models in the Coupled Model Intercomparison Project Phase 5 (CMIP5) do not fully resolve the stratosphere (Flato et al., 2014). The majority of the CMIP6 models examined by Smith et al. (2020) resolve the atmosphere to $>80\text{ km}$ and all compute a stratospheric temperature adjustment. The CMIP6 multi-model ensemble is therefore a more suitable comparison to AIRS measurements. Clear-sky longwave CO_2 ERFs were produced by taking the difference between TOA outgoing clear-sky longwave radiation for CMIP6 $4 \times \text{CO}_2$ and Control model runs and averaging the years after sufficient time elapsed to homogenize atmospheric CO_2 concentration, typically 1 year (Smith et al., 2020). The $4 \times \text{CO}_2$ ERFs were scaled down to $1.1 \times \text{CO}_2$ using the forcing relationship from Etminan et al. (2016) to accord with the atmospheric concentration increase from 2002–2019. The resulting $1.1 \times \text{CO}_2$ ERFs are compared to AIRS measurement in table 1. All CMIP6 climate models predict $0.07\text{-}0.16\text{ W m}^{-2}$ more longwave forcing than is observed. Potential causes of model-observation disagreement are beyond the scope of this work, but it is notable that difference between AIRS observation and the model giving the lowest forcing is approximately the same magnitude as difference between the models giving the highest and lowest forcing.

6 Sources of Error

The unmeasured CO_2 ν_2 wing was assumed to undergo radiance reduction identical to the measured wing, however, $575\text{-}650\text{ cm}^{-1}$ overlaps with stronger water vapor absorption lines. The assumption of symmetry is conservatively high and actual OLR reduction at $575\text{-}650\text{ cm}^{-1}$ is expected to be slightly less than at $687\text{-}765\text{ cm}^{-1}$. Trend asymmetry between the two wings was observed in DLR reported by Feldman et al. (2015): the $575\text{-}650\text{ cm}^{-1}$ wing showed less forcing change over time relative to the $687\text{-}765\text{ cm}^{-1}$ wing, particularly in the southern great plains where atmospheric moisture content is higher.

Over 17 years, detector stability is more important than absolute accuracy as unbiased noise averages to zero over large statistical samples. One possible cause of systematic trend bias is gradual accumulation of molecular contaminants on the AIRS detector mirror. A hypothetical 100 \AA contamination layer is predicted to increase the mirror emissivity variation by 0.001, producing cold scene brightness temperatures at $650\text{-}800\text{ cm}^{-1}$ that are $0.1\text{-}0.2^\circ\text{ K}$ warmer than reality (Aumann et al., 2000). If such a contamination layer were gradually building up during the observation period, warming trends could be amplified and cooling trends (including forcing) could be diminished. Aumann et al. (2018)

Table 1: Longwave clear-sky effective radiative forcing from CMIP6 multi-model ensemble scaled down to $1.1 \times \text{CO}_2$ to compare to AIRS 2002-2019 measurements ($373.13 \rightarrow 410.21$ ppm).

Source	Wm^{-2}	vs AIRS
ACCESS-CM2 (Dix et al., 2020)	0.471	+31%
CanESM5 (Cole et al., 2019)	0.451	+25%
CESM2 (Danabasoglu, 2019)	0.499	+38%
CNRM-CM6-1 (Volz, 2019)	0.459	+27%
CNRM-ESM2-1 (Seferian, 2019)	0.467	+30%
EC-Earth3 (EC-Earth Consortium, 2020)	0.502	+39%
GFDL-CM4 (Paynter et al., 2018a)	0.486	+35%
GFDL-ESM4 (Paynter et al., 2018b)	0.453	+26%
GISS-E2-1-G (NASA Goddard Institute for Space Studies, 2019)	0.495	+37%
HadGEM3-GC31-LL (Andrews, 2019a)	0.460	+28%
IPSL-CM6A-LR (Boucher et al., 2018)	0.463	+28%
MIROC6 (Sekiguchi and Shioyama, 2019)	0.497	+38%
MPI-ESM1-2-LR (Fiedler et al., 2019)	0.509	+41%
MRI-ESM2-0 (Yukimoto et al., 2019)	0.444	+23%
NorESM2-LM (Olivieri et al., 2019)	0.516	+43%
NorESM2-MM (Olivieri et al., 2020)	0.510	+42%
UKESM1-0-LL (Andrews, 2019b)	0.431	+20%
CMIP6 multi-model ensemble average	0.477	+32%
AIRS $-\delta M_{LW}$	0.360 ± 0.026	—%

reported evidence of mirror contamination between 2002-2010 affecting AIRS midwave IR channels ($2181\text{-}2665 \text{ cm}^{-1}$) which were utilized to compute the $\text{CO}_2 \nu_3$ forcing, though this band contributes $<1\%$ to total observed forcing.

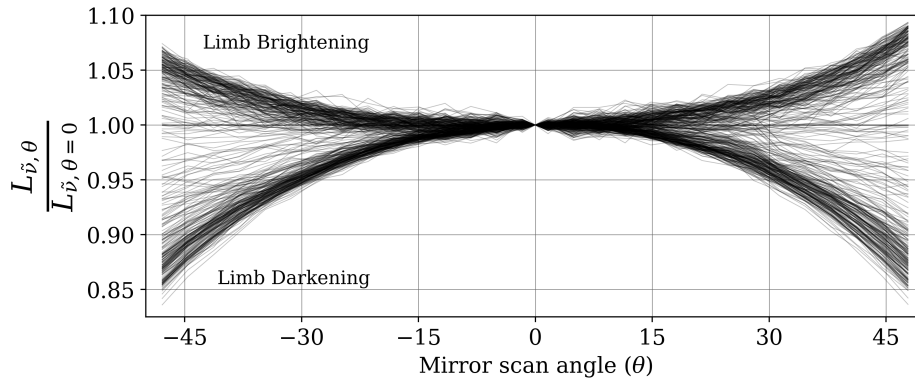


Figure 8: Limb brightening/darkening for $650\text{-}750 \text{ cm}^{-1}$ from granule 004 on Jan 5, 2016. Only radiances at $|\theta| \leq 15^\circ$ were utilized.

This analysis assumed isotropic atmospheric emission when computing radiant exitance change from spectral radiance change. However, high scan angle measurements rarely satisfy the condition of isotropy. Slant path views through an optically-thick atmosphere are subject to significant limb-brightening or limb-darkening. The variation of spectral radiance with scan angle (θ) is apparent upon examining the ratio of $L_{\nu, \theta}$ to the near-simultaneous nadir measurement $L_{\nu, \theta=0}$ at the same wavenumber (figure 8). Over time, if proportionally more (or fewer) high-angle measurements meet the quality and clear-sky selection criteria, trend bias would result. Others have addressed this by applying a computationally-expensive direct integration (Doniki et al., 2015) or by excluding higher scan angle measurements (Aumann et al., 2006; Griggs and Harries, 2007). Given the abundance of data available to this study, the latter approach was adopted and radiances most affected by limb-brightening/darkening at $|\theta| > 15^\circ$ were excluded.

7 Conclusion

Climate models of the Earth energy system may contain errors of opposite signs in different spectral bands that fortuitously compensate, providing satisfactory model agreement for nonphysical reasons (Huang et al., 2007; Etminan et al., 2016). Empirical measurement by hyperspectral satellites provides a means to adjudicate between different climate model RF calculations and promote only those matching reality. Seventeen years of AIRS nighttime, clear-sky OLR measurements reveal $0.360 \pm 0.026 \text{ Wm}^{-2}$ additional longwave radiative forcing induced by +37 ppm atmospheric CO_2 . AIRS lacks measurement capability at $575\text{--}650 \text{ cm}^{-1}$ for complete $\text{CO}_2 v_2$ band characterization, therefore this empirical estimate of increased forcing was devised by presuming $\text{CO}_2 v_2$ wing symmetry and doubling the observed wing's radiative forcing. The latest generation CMIP6 climate models predict $0.431\text{--}0.516 \text{ Wm}^{-2}$ of clear-sky longwave ERF, +20–43% greater than observed by AIRS. Current climate models may require modest revision to bring CO_2 forcing computations into agreement with observation.

References

- John E Harries, Helen E Brindley, Pretty J Sagoo, and Richard J Bantges. Increases in greenhouse forcing inferred from the outgoing longwave radiation spectra of the earth in 1970 and 1997. *Nature*, 410(6826):355, 2001.
- JA Griggs and JE Harries. Comparison of spectrally resolved outgoing longwave radiation over the tropical pacific between 1970 and 2003 using iris, img, and airs. *Journal of climate*, 20(15):3982–4001, 2007.
- Daniel R Feldman, William D Collins, P Johnathan Gero, Margaret S Torn, Eli J Mlawer, and Timothy R Shippert. Observational determination of surface radiative forcing by CO_2 from 2000 to 2010. *Nature*, 519(7543):339, 2015.
- Iouli E Gordon, Laurence S Rothman, Christian Hill, Roman V Kochanov, Y Tan, Peter F Bernath, Manfred Birk, V Boudon, Alain Campargue, KV Chance, et al. The hitran2016 molecular spectroscopic database. *Journal of Quantitative Spectroscopy and Radiative Transfer*, 203:3–69, 2017.
- AIRS Science Team/Joao Teixeira. Aairs/aqua l2 cloud-cleared infrared radiances (airs-only) v006. <https://doi.org/10.5067/Aqua/AIRS/DATA205>, 2013. Accessed 10-2019.
- LL Strow and S DeSouza-Machado. Establishment of airs climate-level radiometric stability using radiance anomaly retrievals of minor gases and sst. *Atmos. Meas. Tech. Discuss*, 2020:1–35, 2020.
- THomas P Charlock. CO_2 induced climatic change and spectral variations in the outgoing terrestrial infrared radiation. *Tellus B: Chemical and Physical Meteorology*, 36(3):139–148, 1984.
- Yi Huang and Venkatachalam Ramaswamy. Evolution and trend of the outgoing longwave radiation spectrum. *Journal of climate*, 22(17):4637–4651, 2009.
- Yi Huang, Stephen Leroy, P Jonathan Gero, John Dykema, and James Anderson. Separation of longwave climate feedbacks from spectral observations. *Journal of Geophysical Research: Atmospheres*, 115(D7), 2010.
- HE Brindley and RJ Bantges. The spectral signature of recent climate change. *Current Climate Change Reports*, 2(3): 112–126, 2016.
- Ed Dlugokencky and Pieter Tans. NOAA/esrl. ftp://afftp.cmdl.noaa.gov/products/trends/co2/co2_mm_gl.txt, 2020. Accessed 07-2020.
- G Myhre, D Shindell, FM Bréon, W Collins, J Fuglestedt, J Huang, D Koch, JF Lamarque, D Lee, B Mendoza, et al. Anthropogenic and natural radiative forcing. climate change 2013: The physical science basis. contribution of working group I to the fifth assessment report of the intergovernmental panel on climate change, 659–740, 2013.
- M Etminan, G Myhre, EJ Highwood, and KP Shine. Radiative forcing of carbon dioxide, methane, and nitrous oxide: A significant revision of the methane radiative forcing. *Geophysical Research Letters*, 43(24):12–614, 2016.
- Gregory Flato, Jochem Marotzke, Babatunde Abiodun, Pascale Braconnot, S Chan Chou, William Collins, Peter Cox, Fatima Driouech, Seita Emori, Veronika Eyring, et al. Evaluation of climate models. In *Climate change 2013: the physical science basis. Contribution of Working Group I to the Fifth Assessment Report of the Intergovernmental Panel on Climate Change*, pages 741–866. Cambridge University Press, 2014.
- Christopher J Smith, Ryan J Kramer, Gunnar Myhre, Kari Alterskjær, William Collins, Adriana Sima, Olivier Boucher, Jean-Louis Dufresne, Pierre Nabat, Martine Michou, et al. Effective radiative forcing and adjustments in cmip6 models. *Atmospheric Chemistry and Physics*, 20(16):9591–9618, 2020.
- Martin Dix, Chloe Mackallah, Doahua Bi, Roger Bodman, Simon Marsland, Harun Rashid, Matthew Woodhouse, and Kelsey Druken. Csiro-arcess access-cm2 model output prepared for cmip6 rf mip piclim-4xco2, 2020. Version 20200428.

- Jason N.S. Cole, Jiangnan Li, Neil Cameron Swart, Viatcheslav V. Kharin, Mike Lazare, John F. Scinocca, Nathan P. Gillett, James Anstey, Vivek Arora, James R. Christian, Yanjun Jiao, Warren G. Lee, Fouad Majaess, Oleg A. Saenko, Christian Seiler, Clint Seinen, Andrew Shao, Larry Solheim, Knut von Salzen, Duo Yang, Barbara Winter, and Michael Sigmond. Ccma canesm5 model output prepared for cmip6 rf mip piclim-4xco2, 2019. Version 20190429.
- Gokhan Danabasoglu. Ncar cesm2 model output prepared for cmip6 rf mip piclim-4xco2, 2019. Version 20190815.
- Aurore Voldoire. Cnrm-cerfacs cnrm-cm6-1 model output prepared for cmip6 rf mip piclim-4xco2, 2019. Version 20190621.
- Roland Seferian. Cnrm-cerfacs cnrm-esm2-1 model output prepared for cmip6 rf mip piclim-4xco2, 2019. Version 20190621.
- EC-Earth Consortium. Ec-earth-consortium ec-earth3 model output prepared for cmip6 rf mip piclim-4xco2, 2020. Version 20200324.
- David J Paynter, Raymond Menzel, Alexandra Jones, Daniel M Schwarzkopf, Stuart Freidenreich, Bruce Wyman, Chris Blanton, Colleen McHugh, Aparna Radhakrishnan, Hans Vahlenkamp, Kristopher Rand, Levi Silvers, Huan Guo, Jasmin G John, Jeffrey Ploshay, V Balaji, and Chandin Wilson. Noaa-gfdl gfdl-cm4 model output prepared for cmip6 rf mip piclim-4xco2, 2018a. Version 20180701.
- David J Paynter, Kristopher Rand, Larry W. Horowitz, Vaishali Naik, Jasmin G. John, Chris Blanton, Colleen McHugh, Aparna Radhakrishnan, Hans Vahlenkamp, and Chandin Wilson. Noaa-gfdl gfdl-esm4 model output prepared for cmip6 rf mip piclim-4xco2, 2018b. Version 20180701.
- NASA Goddard Institute for Space Studies. Nasa-giss giss-e2.1g model output prepared for cmip6 rf mip piclim-4xco2, 2019. Version 20191003.
- Tim Andrews. Mohc hadgem3-gc31-ll model output prepared for cmip6 rf mip piclim-4xco2, 2019a. Version 20191113.
- Olivier Boucher, Sébastien Denvil, Arnaud Caubel, and Marie Alice Foujols. Ipsl ipsl-cm6a-lr model output prepared for cmip6 rf mip piclim-4xco2, 2018. Version 20181204.
- Miho Sekiguchi and Hideo Shiogama. Miroc miroc6 model output prepared for cmip6 rf mip piclim-4xco2, 2019. Version 20190705.
- Stephanie Fiedler, Bjorn Stevens, Karl-Hermann Wieners, Marco Giorgetta, Christian Reick, Johann Jungclaus, Monika Esch, Matthias Bittner, Stephanie Legutke, Martin Schupfner, Fabian Wachsmann, Veronika Gayler, Helmuth Haak, Philipp de Vrese, Stephan Lorenz, Thomas Raddatz, Thorsten Mauritsen, Jin-Song von Storch, Uwe Mikolajewicz, Jörg Behrens, Victor Brovkin, Martin Claussen, Traute Crueger, Irina Fast, Stefan Hagemann, Cathy Hohenegger, Thomas Jahns, Silvia Kloster, Stefan Kinne, Gitta Lasslop, Luis Kornblueh, Jochem Marotzke, Daniela Matei, Katharina Meraner, Kameswarrao Modali, Wolfgang Müller, Julia Nabel, Dirk Notz, Karsten Peters, Robert Pincus, Holger Pohlmann, Julia Pongratz, Sebastian Rast, Hauke Schmidt, Reiner Schnur, Uwe Schulzweida, Katharina Six, Aiko Voigt, and Erich Roeckner. Mpi-m mpi-esm1.2-lr model output prepared for cmip6 rf mip piclim-4xco2, 2019. Version 20190710.
- Seiji Yukimoto, Tsuyoshi Koshiro, Hideaki Kawai, Naga Oshima, Kohei Yoshida, Shogo Urakawa, Hiroyuki Tsujino, Makoto Deushi, Taichu Tanaka, Masahiro Hosaka, Hiromasa Yoshimura, Eiki Shindo, Ryo Mizuta, Masayoshi Ishii, Atsushi Obata, and Yukimasa Adachi. Mri mri-esm2.0 model output prepared for cmip6 rf mip piclim-4xco2, 2019. Version 20200114.
- Dirk Jan Leo Olivieri, Mats Bentsen, ?yvind Seland, Thomas Toniazzo, Ada Gjermundsen, Lise Seland Graff, Jens Boldingh Debernard, Alok Kumar Gupta, Yanchun He, Alf Kirkevåg, Jörg Schwinger, Jerry Tjiputra, Kjetil Schanke Aas, Ingo Bethke, Yuanchao Fan, Jan Griesfeller, Alf Grini, Chuncheng Guo, Mehmet Ilicak, Inger Helene Hafsahl Karset, Oskar Andreas Landgren, Johan Liakka, Kine Onsum Moseid, Aleks Nummelin, Clemens Spensberger, Hui Tang, Zhongshi Zhang, Christoph Heinze, Trond Iversen, and Michael Schulz. Ncc noresm2-lm model output prepared for cmip6 rf mip piclim-4xco2, 2019. Version 20200218.
- Dirk Jan Leo Olivieri, Mats Bentsen, ?yvind Seland, Thomas Toniazzo, Ada Gjermundsen, Lise Seland Graff, Jens Boldingh Debernard, Alok Kumar Gupta, Yanchun He, Alf Kirkevåg, Jörg Schwinger, Jerry Tjiputra, Kjetil Schanke Aas, Ingo Bethke, Yuanchao Fan, Jan Griesfeller, Alf Grini, Chuncheng Guo, Mehmet Ilicak, Inger Helene Hafsahl Karset, Oskar Andreas Landgren, Johan Liakka, Kine Onsum Moseid, Aleks Nummelin, Clemens Spensberger, Hui Tang, Zhongshi Zhang, Christoph Heinze, Trond Iversen, and Michael Schulz. Ncc noresm2-mm model output prepared for cmip6 rf mip piclim-4xco2, 2020. Version 20200206.
- Tim Andrews. Mohc ukesm1.0-ll model output prepared for cmip6 rf mip piclim-4xco2, 2019b. Version 20200410.
- HH Aumann, D Gregorich, S Gaiser, D Hagan, T Pagano, L Strow, and D Ting. Airs algorithm theoretical basis document. *Level 1B, Part, 1:70*, 2000.

-
- Hartmut H Aumann, Evan M Manning, and Steve Broberg. Radiometric stability in 16 years of airs hyperspectral infrared data. volume 10764, page 1076400. International Society for Optics and Photonics, 2018.
- Stamatia Doniki, Daniel Hurtmans, Lieven Clarisse, Cathy Clerbaux, Helen M Worden, Kevin W Bowman, and Pierre-François Coheur. Instantaneous longwave radiative impact of ozone: an application on iasi/metop observations. 2015.
- HH Aumann, Steve Broberg, Denis Elliott, Steve Gaiser, and Dave Gregorich. Three years of atmospheric infrared sounder radiometric calibration validation using sea surface temperatures. *Journal of Geophysical Research: Atmospheres*, 111(D16), 2006.
- Yi Huang, V Ramaswamy, Xianglei Huang, Qiang Fu, and Charles Bardeen. A strict test in climate modeling with spectrally resolved radiances: Gcm simulation versus airs observations. *Geophysical Research Letters*, 34(24), 2007.